

A Measurement-Based Spatially Consistent Channel Model for Distributed MIMO in Industrial Environments

Christian Nelson, *Student Member, IEEE*, Sara Willhammar, *Member, IEEE*, and Fredrik Tufvesson, *Fellow, IEEE*.

Abstract—Future wireless communication systems are envisioned to support ultra-reliable and low-latency communication (URLLC), which will enable new applications such as compute offloading, wireless real-time control, and reliable monitoring. Distributed multiple-input multiple-output (D-MIMO) is one of the most promising technologies for delivering URLLC. This paper classifies obstruction and derives a channel model from a D-MIMO measurement campaign carried out at a carrier frequency of 3.75 GHz with a bandwidth of 35 MHz using twelve distributed fully coherent dipole antennas in an industrial environment. Channel characteristics are investigated, including statistical measures such as small-scale fading, large-scale fading, delay spread, and transition rates between line-of-sight and obstructed line-of-sight conditions for the different antenna elements, laying the foundations for an accurate channel model for D-MIMO systems in industrial environments. Furthermore, correlations of large-scale fading between antennas, spatial correlation, and tail distributions are included to enable proper evaluations of reliability and rare events. Based on the results, a channel model for D-MIMO in industrial environments is presented together with a recipe for its implementation.

Index Terms—channel characteristics, channel model, D-MIMO, industry, IoT, measurements, URLLC.

I. INTRODUCTION

FUTURE wireless systems are required to support the ultra-reliable low-latency communication (URLLC) use case for applications such as remote driving and industrial automation. In addition to URLLC, the latter also needs functionality such as localization, sensing, and being able to support energy-neutral devices, to name a few [1]. As part of enabling these functionalities and meeting the use case and application requirements, there is a technological shift towards distributed compute capabilities and distributed multiple-input multiple-output (D-MIMO) systems [2].

The shift to more distributed antenna systems has a large potential to increase the reliability of wireless communication systems. Increasing the number of antennas in a MIMO system has been shown to improve reliability by decreasing small-scale fading, through the so-called channel hardening effect [3]. Distributed antenna systems have the potential to further improve the stability of the system, as they will also

reduce large-scale fading [4], [5]. This is because there will be – with high probability – one or several access points close by, often experiencing different large-scale fading effects. Decreasing these two types of fading effects not only improve the reliability but also reduce the required transmit power and fading margins.

To develop new systems, use cases, functionalities and products and to reduce development costs and shorten the time to market, simulations are an important tool. In order for these simulations to give accurate and realistic results, the underlying channel model needs to capture the essential characteristics of the channel. For D-MIMO systems, correlations of large-scale fading is of special interest.

A fully deterministic ray-tracer would give an accurate result, but restricted to a specific environment. Adding stochastic elements to the ray-tracer would generalize the results, while still being spatially consistent such that, e.g. sensing algorithms can be verified. On the other hand, a completely stochastic channel model that relies on extracted channel parameters such as channel gain and Doppler spectrum, can be used. However, then the challenge is to get a physical correspondence for sensing and localization algorithms and to model non-stationarities. Therefore, a hybrid model, or a geometry-based stochastic channel model is preferred.

To ensure that the essential characteristics of the channel for the target scenario are captured, measurements must be made. Wireless channels in industrial environments have been measured and modeled for decades [5]–[10]. However, as system architectures evolve, and how the channel is experienced depends on the interaction with the system, there is a need for new channel models. In the 3GPP technical report 38.901 Rel. 18 [11], general propagation channel models for indoor factories are presented.

In [12], [13], measurement-based comparisons were made between different antenna configurations, i.e. co-located massive multiple-input multiple-output (MIMO) and distributed antennas. In [12], the scenarios are static and only the received signal strength (RSS) is presented to evaluate the coverage. The authors also investigate how the different configurations compare when a maximum ratio precoder is used to beamform to a user, and how much is leaked to other idle users. [13] performed a similar analysis but instead focused on the achievable downlink spectral efficiency. In another static indoor distributed setup, a measurement-based estimation of the large-scale parameters and its spatial consistency was carried out and the path gain and the large-scale fading were

Christian Nelson, Sara Willhammar and Fredrik Tufvesson are with the Department of Electrical and Information Technology, Lund University, Lund, Sweden. Email: first.name.last.name@eit.lth.se

This work has been sponsored by the European Union’s Horizon 2020 research and innovation program under grant agreement No 101013425 (project “REINDEER”), and by the Excellence Center at Linköping – Lund in Information Technology (ELLIIT).

Manuscript received Dec. 17, 2024; revised MM XX, 2025.



Fig. 1. The rich scattering and heavily shadowed industrial environment where the D-MIMO measurements were conducted.

simultaneously modeled using a Gaussian process [14]. There, small-scale fading was not considered.

In this work, we have conducted a unique measurement campaign with a D-MIMO system in an industrial environment [15]. We are presenting a new approach of how to classify obstruction in D-MIMO systems, we are investigating spatial and temporal non-stationarities as well as extracting key parameters such as fading characteristics in order to create an accurate, yet simple, measurement-based spatially consistent channel model, which can be used for realistic system simulations of D-MIMO systems in industrial scenarios.

The paper is structured as follows. First in Section II, the measurement equipment and environment is introduced. Then in Section III, we are classifying obstruction as caused by the environment, classifying samples as line-of-sight (LoS) and obstructed line-of-sight (OLoS). From that we compute the path gain in Section IV and large-scale fading parameters in Section V. This is followed by Section VI, which includes an analysis of the small-scale fading statistics, where the local scattering function and collinearity are computed to get to the appropriate stationarity regions. Finally, in Section VII, a channel model recipe for how to generate spatially consistent D-MIMO channels in industrial environments is presented, before conclusions are given in Section VIII.

Notation: Column vectors and matrices are denoted by boldface lowercase, \mathbf{x} , and uppercase letters, \mathbf{X} , respectively. The operator $\text{vec} : \mathbf{X} \mapsto \mathbf{x}$ vectorizes the matrix \mathbf{X} by stacking its columns on top of each other into \mathbf{x} . $(\cdot)^\top$ and $(\cdot)^H$ denote the transpose and the Hermitian transpose of (\cdot) , respectively. The Euclidean norm of \mathbf{x} is $\|\mathbf{x}\|$. The $N \times N$ identity matrix is denoted as \mathbf{I} , where the size is implicit from the context. Also implicit from the context, $\mathbf{1}$ is the column vector where all elements are 1. Lastly, $[\mathbf{X}]_{m,n}$ is the element in the m -th row and n -th column.

II. MEASUREMENT SCENARIO

The measurement campaign was carried out in an industrial environment at the department of mechanical engineering at Lund University. The channel sounder presented in [15] was used to collect the samples at a carrier frequency of $f_c = 3.75$ GHz, utilizing a bandwidth of 35 MHz distributed over $N_f = 449$ tones, resulting in a carrier spacing of 78.125 kHz.

The sounder is designed for D-MIMO measurements and captures all possible link combinations that later can be used for offline processing and analysis. All included radio units share the same notion of time through a distributed 1 pulse-per-second (1PPS) signal, and are frequency disciplined with external coherent rubidium (Rb) clocks.

The environment in which the channel samples were collected is depicted in Fig. 1, from which it is clear that it is a rich scattering environment with many metallic objects and structures, causing both reflections and shadowing. As shown in Fig. 2, the dimensions of the room are approximately 30 m long and 12 m wide, with a 8 m height to the ceiling. The access points, here called anchors, were mounted on rails approximately 4 m above the floor with antennas tilted downward to cover the center of the hall.

At each anchor, the output of the sounder is a channel vector $\tilde{\mathbf{h}}_k^{(m)} \in \mathbb{C}^{N_r \times 1}$, at time k and from anchor m , which is an estimate of the true channel transfer function, but corrupted by noise. For this campaign, $m \in \{1, 2, \dots, 12\}$ and $k \in \{0, 1, \dots, N_t - 1\}$. All captured channel transfer functions from a measurement is collected in the matrix

$$\mathbf{H}^{(m)} = \left[\tilde{\mathbf{h}}_0^{(m)}, \dots, \tilde{\mathbf{h}}_{N_t-1}^{(m)} \right] \in \mathbb{C}^{N_r \times N_t} \quad (1)$$

for further processing. The agent moving in the environment was a remotely controlled robot that carried all the necessary radio equipment. To obtain an estimate of the ground truth position of the agent in the map during the measurements, the agent was equipped with a light detection and ranging (lidar) and an inertial measurement unit (IMU) to perform offline simultaneous localization and mapping (SLAM) [16]. A more detailed list and description of the equipment can be found in [15].

Here, five measurements are presented covering three different scenarios, as visualized in Fig. 2. The three scenarios are: 1) the ref scenario where the agent was driving back and forth in the middle of the hall at a speed of approximately 0.8 m/s, 2) the loop scenario where the agent was driving two laps around machinery (parts of the loop is in a section of the industry hall where the ceiling is considerably lower, which will lead to a challenging radio channel environment with a lot of obstruction), and 3) the scan scenario where the agent is driving around in order to cover the majority of the accessible hall, including in between machines. With 449 active tones, for 5 measurements, each with a length between 60 s and 240 s, the result is 1 440 000 recorded channel transfer functions. The raw data are available at [17].

III. CLASSIFYING OBSTRUCTION

In D-MIMO systems, it is likely that one or more anchors are in LoS, while others are in OLoS. To investigate how likely it is to be in one state or the other, the obstruction is classified in the following section. An approximation of the obstruction of the first Fresnel zone can be derived from the lidar data and used for the purpose of state classification. As a result of this, the coverage of the first Fresnel zone is seen in Fig. 3 for the loop scenario in Fig. 2. There are variations over time, where the link between the agent and an anchor

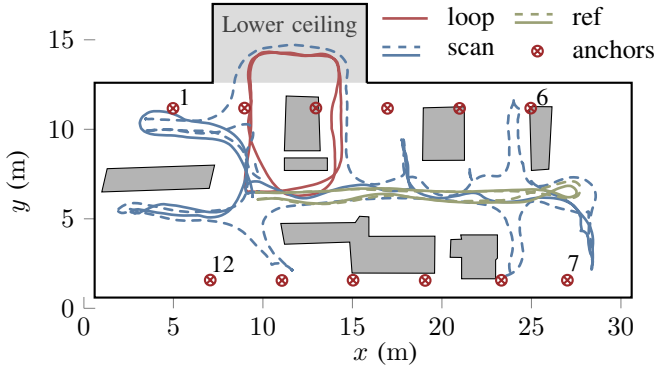


Fig. 2. Top-down overview of the industrial environment where the D-MIMO measurements were conducted. The anchors are visible along the two sides and the trajectories driven by the agent are visualized. The numerology of the anchors is shown for anchors 1, 6, 7, and 12; the rest are implicit for visual purposes. The solid and dashed lines represent different measurement runs, i.e. measurements captured during different times.

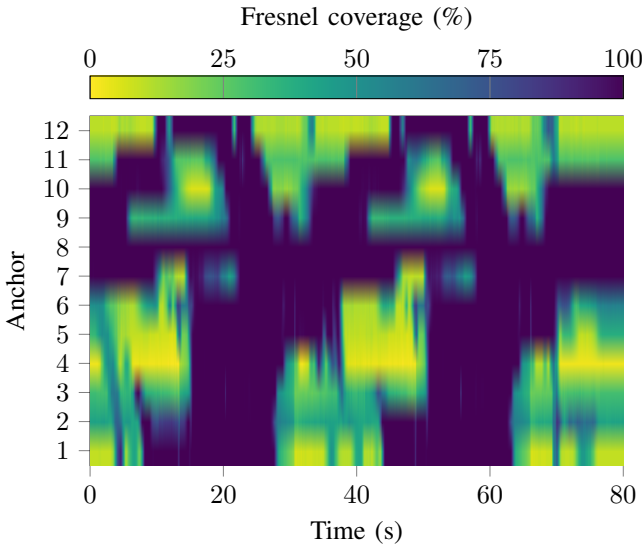


Fig. 3. The amount of the approximated first Fresnel ellipse that has obstruction inside it, resulting in the Fresnel coverage, over time and for all anchors. The scenario depicted is the loop scenario (—).

is more or less obstructed. At each time instant at least some anchors have a more or less line-of-sight (LoS) link, i.e. a low number of the Fresnel coverage, while some are obstructed. As an example of the latter, anchor 8 is always obstructed with a Fresnel coverage of 100%. It is also clear that when the agent is driving into the section with a lower ceiling, the LoS is completely obstructed to all the anchors on one side of the room.

The Fresnel coverage was computed as follows. The output from the SLAM algorithm provides the ground-truth trajectory of the agent and a three-dimensional (3D) point cloud representation of the environment, i.e. a map. With these data, the obstruction of the first Fresnel zone can be approximated, as elaborated on in the following. In each time step k , and for each anchor m , the line between the agent and the anchor m is drawn. Then all 3D lidar points that have a distance to the line that is less than a given radii r are saved. Those lidar points

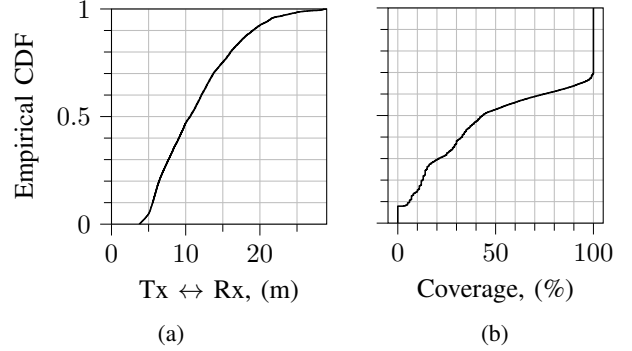


Fig. 4. (a) The distribution of the anchor and agent separation, and (b) the CDF of the approximated coverage of the first Fresnel zone.

are then projected onto a circle in the cylinder. Choosing the radii r related to the size of the first Fresnel zone enables the derivation of a metric of the fraction of the circle area that is covered with lidar points, i.e. objects in the environment. This is an approximation of how much obstruction there is between the anchor m and the agent at time k , that is, the Fresnel coverage. Let $\mathbf{LOS} \in \mathbb{R}^{M \times N_t}$ denote the coverage of the circle at time k for link m where $[\mathbf{LOS}]_{m,k} \in [0, 100]$. Since the approximation of the first Fresnel zone depends on the cylinder radii, the radii of the Fresnel ellipse was determined for a distance of 5 m. This choice was based on the fact that all machinery was located along the walls, close to the anchors. Furthermore, to be less sensitive to noise in the lidar scans, a manual investigation of the radii was also conducted. Then the radii were chosen as $r = 2\lambda$.

The empirical cumulative distribution function (ECDF) for the distances between agent (Tx) and anchor (Rx) is shown in Fig. 4a and the CDF of the approximated coverage of the first Fresnel zone is shown in Fig. 4b. Due to the environment and deployment, it is rare that the distance between the agent and an anchor is above 20 m, as depicted in Fig. 4a. In the ECDF in Fig. 4b it can be seen that this is a challenging environment where the links in the data set are in a fully obstructed LoS (OLOs) state more than 30% of the time.

The data is classified into two states. One in which the coverage (or obstruction) lies between 0% to 50%, and another in which the coverage is in the range 50% to 100%. The states are named LoS and OLoS, respectively. For completeness, it should be mentioned that we also evaluated the case with three states (LoS, OLoS and non-line-of-sight (NLoS)), but there were no major differences in the statistics that would motivate this more complex classification and modeling approach. Hence, the matrix $\mathbf{H}^{(m)}$ is split into the matrices $\mathbf{H}_{\text{LoS}}^{(m)}$ and $\mathbf{H}_{\text{OLOs}}^{(m)}$, where the difference between two consecutive time indices no longer need to be equal, i.e.,

$$\mathbf{H}_{\text{LoS}}^{(m)} = \left[\tilde{\mathbf{h}}_k^{(m)} \mid k \in \{0, \dots, N_t - 1\} : [\mathbf{LOS}]_{m,k} \leq 50 \right], \quad (2)$$

and

$$\mathbf{H}_{\text{OLOs}}^{(m)} = \left[\tilde{\mathbf{h}}_k^{(m)} \mid k \in \{0, \dots, N_t - 1\} : [\mathbf{LOS}]_{m,k} \geq 50 \right]. \quad (3)$$

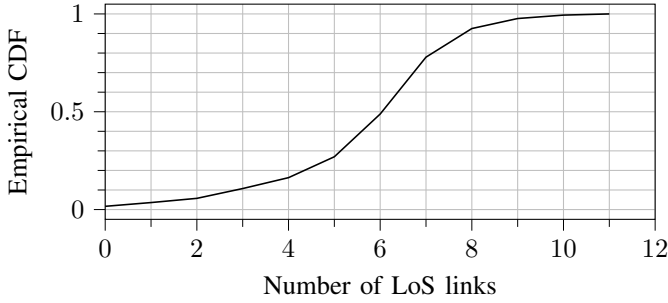


Fig. 5. The ECDF of the number of links with LoS conditions throughout the measurements.

A. Line-of-sight probability

Having classified the obstruction and divided the data set into LoS and OLoS, the next steps include computing the probability of LoS and the probabilities of a change of state. As a starting point, to get a better understanding of what constitutes real D-MIMO channels in heavily shadowed industrial environments, the distribution of the number of LoS links in each time instance is shown in Fig. 5. It can be observed that in this scenario there are never twelve links in LoS condition at the same time. However, there is also a low probability that there are zero links in LoS, which is promising from a reliability perspective. In these measurements, there are six antennas (50% of the total number) with the LoS condition, 50% of time. In the following, the average number of state

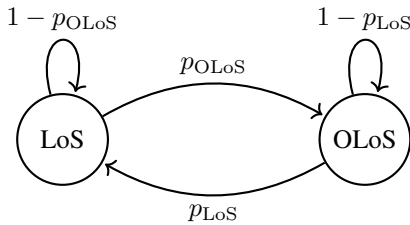


Fig. 6. State transition graph, including the probability to stay in LoS and OLoS as well as to change to OLoS and to LoS from the respective state.

transitions per distance traveled is estimated; that is, how often a link alternates between states LoS and OLoS. These two states are visualized in Fig. 6, where a transition between states occurs with a probability p_s , then the probability of staying in a certain state is $1 - p_s$, for $s \in \{\text{LoS}, \text{OLoS}\}$. Each anchor m has its own probabilities for the transitions. These probabilities can be modeled using an Exponential distribution, $\text{Exp}(\lambda_s^{(m)})$, with the rate parameter $\lambda_s^{(m)} \in U(0.04, 0.22)$, measured in the unit of transitions per meter traveled by the agent. Assuming that the probability for the state transition is not equal, λ was computed for the two states separately. However, this investigation showed only minor differences in the parameters, concluding that the uniform distribution with parameter limits 0.04 and 0.22 was suitable for both states. For reference, in this scenario, the average distance that an anchor is classified as LoS is 4.65 m and for OLoS the corresponding value was 5.55 m.

IV. PATH GAIN

Having the obstruction classification and state transition probability in place, the next step is to model the distance-dependent path gain for the two states. Starting by averaging the channel power gains over the tones as in

$$\bar{\mathbf{P}}^{(m)} = \frac{1}{N_f} \mathbf{1}^\top |\mathbf{H}^{(m)}|^2 \in \mathbb{R}^{1 \times N_t}, \quad (4)$$

and then collecting the averaged power gains from all anchors m in the matrix

$$\bar{\mathbf{P}} = [\bar{\mathbf{P}}^{(1)\top}, \dots, \bar{\mathbf{P}}^{(M)\top}] \in \mathbb{R}^{N_t \times M}, \quad (5)$$

then the matrix

$$\mathbf{d} = [\mathbf{d}^{(1)}, \dots, \mathbf{d}^{(M)}] \in \mathbb{R}^{N_t \times M} \quad (6)$$

contains the distances from the agent to all the anchors, where the distribution of the distances across all measurements is shown in Fig. 4a. Vectorizing the matrices

$$\text{vec } \bar{\mathbf{P}} \in \mathbb{R}^{MN_t \times 1} \quad \text{and} \quad \text{vec } \mathbf{d} \in \mathbb{R}^{MN_t \times 1} \quad (7)$$

and sorting them simultaneously leads to a monotonically increasing $\text{vec } \mathbf{d}$. Since the channel coefficients in $\mathbf{H}^{(m)}$ contain the influence from the antennas (and its antenna gain pattern), all points closer than $2.65 \cdot \sqrt{2}$ meters are removed when estimating the path gain parameters. This due to that distances closer than this will drastically effect the results due to the large drop in gain due to the combined antenna patterns from the agent and the anchor. The log-distance results for both the LoS and OLoS state are shown in Fig. 7, where the gray dots are the discarded measurement points. The minimum mean square error (MMSE) lines in red are computed as

$$\text{PG}(d) = \begin{cases} -44.24 - 0.86 \cdot 10 \log_{10}(d/d_0), & \text{LoS}, \\ -48.78 - 0.95 \cdot 10 \log_{10}(d/d_0), & \text{OLoS}. \end{cases} \quad (8)$$

for all distances $d \in [2.65 \cdot \sqrt{2}, 30]$ meters. The reference distance is set at $d_0 = 1$ m. As seen in Fig. 7, the LoS data set has in general a higher channel gain and the measurement points show smaller variations around the MMSE line, in comparison to the OLoS data set. The exponents are relatively small compared to other measurements that have been performed over the years [7], [18], which could be a result of the rich scattering and the relatively short link distances and that the antennas are considered a part of the channel in this data set. The combined antenna gain patterns from the anchors and the agent also makes the slope less steep.

In further inspection of Figs. 4a and 7, it can be concluded that the distribution of distances in the measurements is not even; some distances have significantly more samples than others and will therefore have a higher weighting in the MMSE computation. Hence, as an attempt to address this and give all distances equal weight, the logarithmic distances were binned into 1000 equally spaced bins. In each bin, the average channel power gain was extracted, and then these 1000 points were used to estimate the path gain parameters. Then the points closer to the anchors get a larger weight, leading to slightly larger exponents and a shift of the slope. As a result, the path gain was no longer in the center of the points; or in other

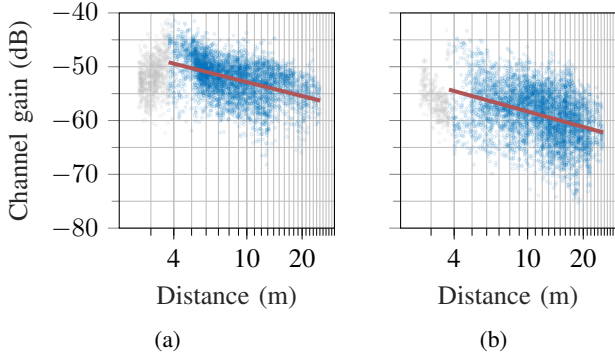


Fig. 7. The channel power gains and the corresponding linear model for the (a) LoS and (b) OLoS data sets, respectively. The gray points are discarded measurements due to the large impact of the combined antenna gain patterns. Note that only every 150th point is shown in the plot for clarity .

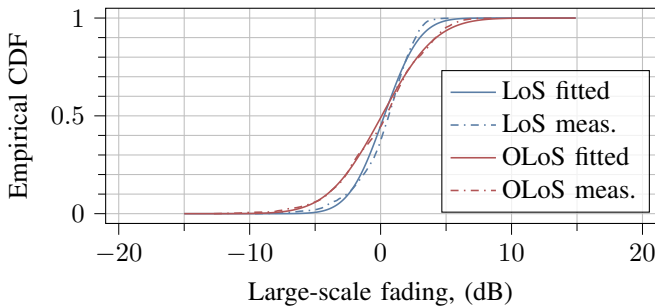


Fig. 8. The ECDF of the large-scale fading with the corresponding fitted log-normal distribution, for the LoS and OLoS data set, respectively.

words, the mean had shifted, leading to the fact that the mean in the large-scale fading in later analysis was no longer (close to) zero. Therefore, for modeling purposes, the complete data set is used in the analysis, without binning.

V. LARGE-SCALE FADING

To estimate large-scale fading, the distance-dependent path gain in (8) is subtracted from the average power gain (5), i.e. $\bar{P} - \mathbf{P}\mathbf{G}(d)$. A moving average window with a length of approximately 10λ is applied to estimate large-scale fading [19]. The resulting distribution of the large-scale fading follows a log-normal distribution and the empirical CDF of the estimated large-scale fading with the corresponding fitted distributions are shown in Fig. 8, for both the LoS and OLoS data sets. The means for the two distributions are not exactly zero, but close enough such that for model simplicity, they are assumed to be zero with their respective variances. The mean and standard deviation for the LoS data set is 0.27 and 2.13, respectively, and the corresponding values are 0.08 and 3.25 for the OLoS data set. As expected, the variations for the OLoS case is slightly larger.

A. Covariance

For distributed systems, the correlation of large-scale parameters becomes important, as it will affect system performance [20], [21]. The sample reflective correlation is used here to compute the covariance of large-scale fading between

the anchors; this is equivalent to the cosine similarity, i.e. the mean is not removed. The correlation between anchors x and y can be calculated using

$$\rho_{xy} = \frac{\sum x_i y_i}{\sqrt{\sum x_i^2} \sqrt{\sum y_i^2}}. \quad (9)$$

The resulting covariance of large-scale fading between all anchors can be seen in Fig. 9 for the LoS and the OLoS data sets, respectively. Naturally, the diagonal in both cases is one. In the LoS data set there are not enough LoS links between anchor 7, 8 and 9 to compute their correlation; hence the white spaces. One general observation is that the covariances are smaller in the LoS data set than in the OLoS data set; the main exception being anchors 10, 11 and 12, which tend to have more similar statistics in LoS.

For the OLoS data set, the covariance of the large-scale fading is more prominent. This can especially be observed between anchors situated on the same side of the wall and even more for anchors 1-6, which seem to be interacting with the same objects at the same time, leading to that they experience similar large-scale fading behavior. The cross-correlation between anchors on opposite sides tends to have smaller values; a tendency that can also be observed in the LoS data set, although not as prominent.

After evaluation, the covariance matrices for the states LoS and OLoS are modeled as truncated normal distributions. Both distributions are truncated at -0.9 and 0.9 . The elements of the covariance matrix are drawn from $\mathcal{N}(0.1, 0.4)$ for LoS, and $\mathcal{N}(0.5, 0.5)$ for OLoS.

B. Auto-correlation

Having evaluated the instantaneous covariance between anchors, in the following section, the auto-correlation $R_{xx}^{(m)}$ of the large-scale fading per anchor was explored. For the two data sets the auto-correlation was computed for all anchors and the value of the forgetting factor k was estimated in the following [22]

$$R_{xx}^{(m)}(d) = e^{-kd}. \quad (10)$$

The result in the LoS data set is a k of 0.82 and in the OLoS data set $k = 0.81$. Defining $R_{xx}(d) = 1/e$ as the decorrelation distance leads to $d_{1/e}$ for the LoS data set to 1.22 m and for OLoS it is 1.24 m.

VI. SMALL-SCALE FADING

To get the small-scale fading statistics, one first has to define the regions where the channel can be considered as wide-sense stationary and uncorrelated scatterers (WSSUS). This is done through the local scattering function and by analyzing the collinearity.

A. The Local Scattering Function

The local scattering function is typically used to characterize dynamic (non-stationary) channels [23], [24]. When moving in a rich scattering and heavily shadowed environment, such as the industrial hall presented here, one might violate the WSSUS assumption conventionally used, if considering the

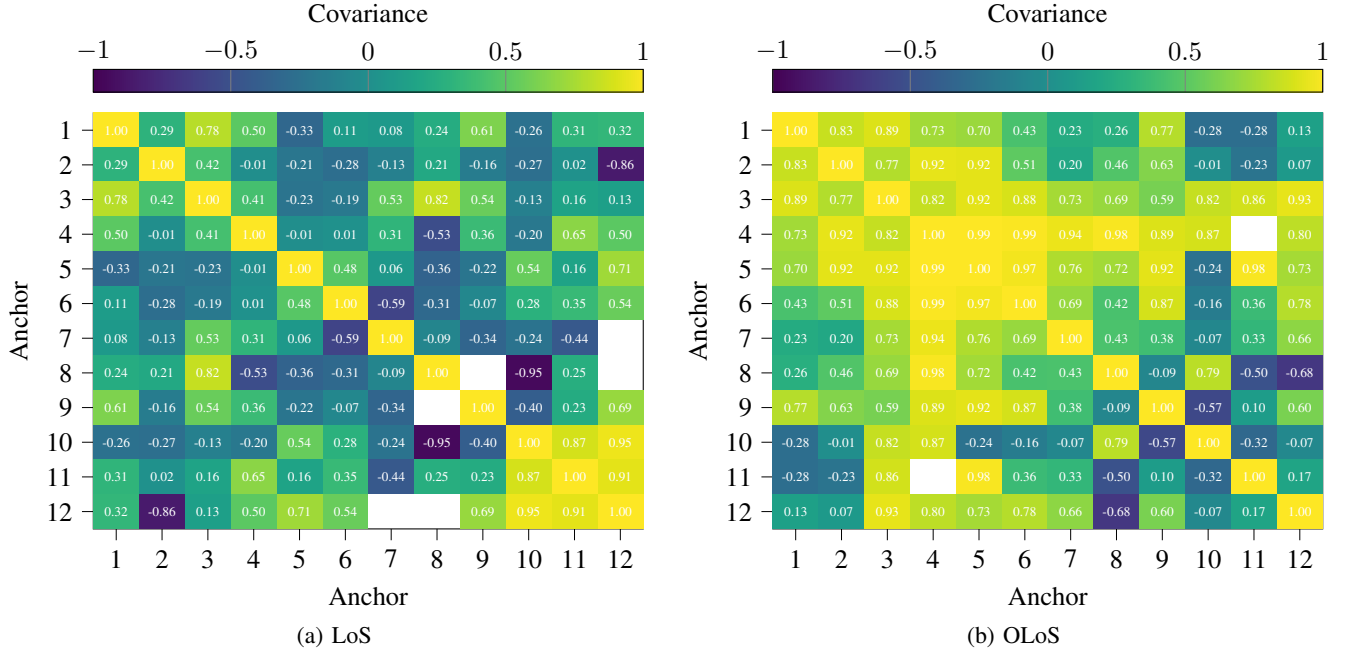


Fig. 9. The covariance of the large-scale fading for LoS and OLoS data. Each entry in the matrix has been estimated pairwise to get enough data. Note that there are never enough simultaneous LoS links between the agent and anchors 8 and 12.

entire data set at once. By treating the channel as a piece-wise stationary stochastic process – i.e. the data is windowed into smaller parts where the WSSUS assumptions approximately hold – it is possible to extract the channel parameters in this local region. The local scattering function solves the problem by applying a time- and frequency-bound filter that moves over the data set. Following the methodology presented in [24], the sliding window indices in time and frequency are denoted as k_t and k_f , respectively, and the size of the windows in time and frequency are denoted as K and N , respectively. Following [25], $N = N_f$ and dropping the index k_f , the local scattering function for anchor m at index time k_t , is estimated as

$$\mathbf{C}_{k_t}^{(m)} = \frac{1}{IJ} \sum_{w=0}^{IJ-1} \left| \mathbf{W}_{k_t}^{(w;m)} \right|^2. \quad (11)$$

In (11), the matrix $\mathbf{W}_{k_t}^{(w;m)}$ is the filtered channel matrix using the I and J separable band-limited discrete prolate spheroidal sequences: I sequences in the frequency domain, and J sequences in the time domain. For details, see [15] where the relations between indices and matrices are explained thoroughly. For the analysis performed here, the parameters I and J were chosen as $I = 1$ sequence over frequency and $J = 2$ sequences over time. The length K of the window was first set to 150 to analyze the stationarity length in which the channel statistics is assumed to be wide-sense stationary. An overlap of the window of 50% was used.

From the local scattering function it is straightforward to derive the power delay profile (PDP) and Doppler spectral density (DSD) as the marginal expectations over the corresponding dimension. When calculating the root mean square (RMS) delay spread, the moments of the PDP need to be calculated. To obtain accurate estimates of the RMS delay

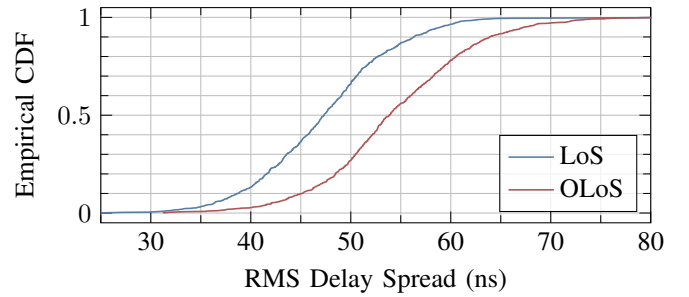


Fig. 10. The root-mean square delay spread for the LoS and OLoS data sets.

spread, only contributions from the PDP that exceed certain power thresholds should be considered [26]. The thresholds were selected as 5 dB above the noise floor to mitigate spurious peaks, and 40 dB below the PDP peak to only consider components with significant contributions. The empirical CDF for the RMS delay spread is shown in Fig. 10 for the LoS and OLoS data sets, respectively. The delay spread is naturally smaller in LoS than in OLoS, with median values of 47 and 53 ns, respectively.

B. Collinearity

Using the collinearity metric between the local scattering functions at two different time instances k_t and k_t' , results in a quantity of how similar the statistics are at the two different instances and, in extension, how long the stationarity region is. The collinearity metric $R(k_t, k_t')$ is defined as

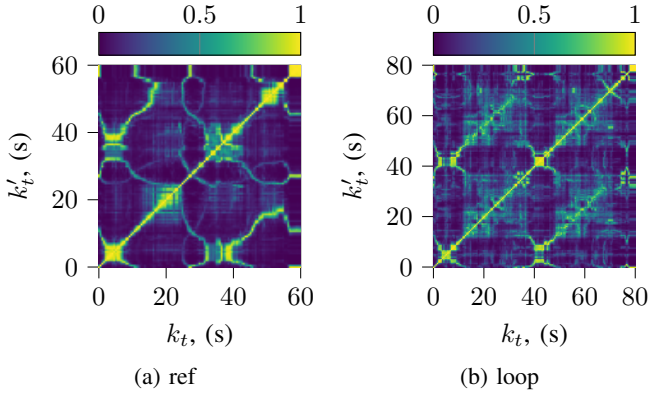


Fig. 11. The collinearity matrix for two of the measured scenarios; ref and loop. Both plots depict the collinearity between the agent and anchor 4.

$$R(k_t, k'_t) = \frac{(\text{vec } \mathbf{C}_{k_t}^{(m)})^\top (\text{vec } \mathbf{C}_{k'_t}^{(m)})}{\|\text{vec } \mathbf{C}_{k_t}^{(m)}\| \cdot \|\text{vec } \mathbf{C}_{k'_t}^{(m)}\|}, \quad (12)$$

where \mathbf{C} represents the local scattering function in (11). The collinearity between the agent and anchor 4 from the ref and loop scenario are shown in Fig. 11. Anchor 4 is chosen for illustrative purpose, but the analysis holds for every anchor. All the elements of the resulting collinearity matrix are between zero and one (the diagonal is always one). In Fig. 11a, where the agent was driving back and forth in the middle of the hall, there is a symmetry for $k_t + k'_t > 55$, which is when the agent is turning and starts driving back to the start position. In Fig. 11b, where the agent is driving two laps around machinery, it can also be clearly seen when the agent are close to the starting position after one lap and then how there is a parallel line approximately with a constant 40s separation. A threshold needs to be set in order to decide how similar the statistics needs to be in order to be considered WSSUS. Defining the indicator function as

$$\gamma(k_t, k'_t) = \begin{cases} 1 & : R(k_t, k'_t) > c_{\text{th}}, \\ 0 & : \text{otherwise}, \end{cases} \quad (13)$$

where c_{th} defines the threshold. Following [24], the threshold was chosen as 0.9. The indicator function (13) is applied to the collinearity results in a binary matrix with ones on the diagonal. The width of the region around the diagonal then gives the stationarity time. Multiplying the stationarity region (expressed in seconds) by the average velocity of the agent, the stationarity distance can be acquired. That is, the distance for which the WSSUS assumption (approximately) holds. The empirical CDF of the stationarity distance is plotted in Fig. 12 for the LoS and OLoS data sets. It is clear that the median distance is on the order of 1 m for the LoS data set, and slightly shorter for the OLoS data set. Based on these stationarity distances, a window length of 300 snapshots (1.5 s) is selected when extracting the statistics in the remaining. Since the maximum instantaneous velocity of the agent was about 0.8 m/s, the maximum length traveled during 300 snapshots approximately equals 1.6 m, but is usually somewhat shorter.

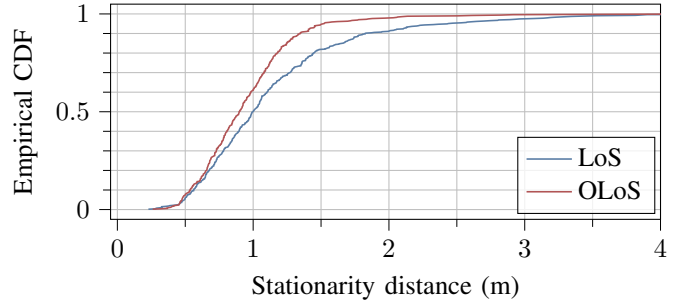


Fig. 12. The empirical CDF of the estimated stationarity distance for the LoS and OLoS data sets, when the collinearity threshold was selected to be $c_{\text{th}} = 0.9$.

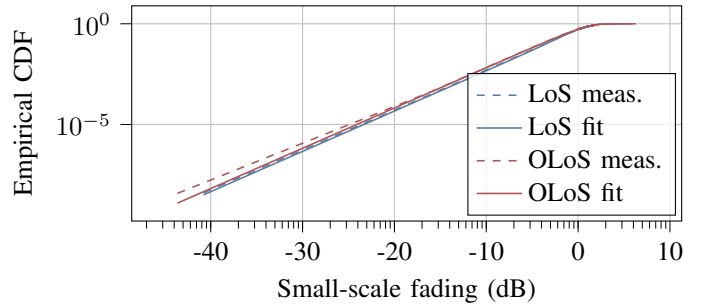


Fig. 13. The small-scale fading of the LoS and OLoS data sets. Depicted are the empirical CDF and their Ricean fitted distributions.

C. Small-scale fading statistics

To get an estimate of the small-scale averaged amplitude of $\mathbf{A}^{(m)} = |\mathbf{H}^{(m)}|$, a moving average window of length $K = 300$ was applied over the time dimension, for all tones, resulting in an estimate of the small-scale fading $\mathbf{A}_{\text{SSA}}^{(m)} \in \mathbb{R}^{N_f \times N_t - K + 1}$. The length K of the window should be approximately 10λ [19], but due to the dynamic nature of the measured scenario, the value of K will also change over time. The estimate of the small-scale fading, $\mathbf{A}_{\text{SSF}}^{(m)}$, is then given as

$$\mathbf{A}_{\text{SSF}}^{(m)} = \mathbf{A}^{(m)} \odot \frac{1}{\mathbf{A}_{\text{SSA}}^{(m)}}, \in \mathbb{R}^{N_f \times N_t - K + 1}, \quad (14)$$

where $1/\mathbf{A}_{\text{SSA}}^{(m)}$ is the element-wise inversion under the assumption that non of the elements in $\mathbf{A}_{\text{SSA}}^{(m)}$ are zero. The empirical CDF of the small-scale fading, for the two data sets, is shown in Fig. 13 along with its Ricean fit that follows the measured curves. It is noteworthy that the small-scale fading shows similar behavior in the two data sets. The small-scale fading in the LoS data set can be modelled as Rice (0.84, 0.49) which gives a K -factor of 1.44. For the OLoS case, the distribution is modeled as a Rice (0.72, 0.59) distribution with a K -factor of 0.74. The reason for the low K -factor in the LoS data set as well as the fact that there is a (although small) K -factor in the OLoS data set could be consequences of the classification of obstruction and/or be attributed to the short link distances and rich scattering environment that could result in several strong multipath components.

D. Channel hardening

One key advantage of deploying (massive) MIMO systems is the channel hardening effect. In essence, it means that MIMO can combat small-scale fading, mitigating fading dips due to destructive superpositioning of multipath components. When the number of antennas M is increasing, linear schemes such as maximum ratio transmission (MRT) have been shown to become optimal [27]. This effect can be very prominent in massive MIMO channels in rich scattering environments [5]. Although the system here can not be considered to be massive MIMO, but rather consisting of twelve distributed antennas, it is still shown in the following that there is a significant channel hardening effect.

In [5], the channel hardening for a distributed MIMO setup was measured in a limited area in a fully OLoS scenario where channel parameters such as large-scale fading can be assumed to be constant. Also, the distribution of the M antennas are on a wall roughly $10\text{ m} \times 3\text{ m}$ (W x H), which will not drastically influence the distance-dependent path gain. In that setting, the complex channel gains can be modeled as independent and identically distributed (i.i.d.) complex Gaussian with no dominant component, which leads to a Rayleigh distribution of the channel gain amplitudes, and in extension, the channel power gains become exponentially distributed. Furthermore, performing MRT – which translates to the sum of channel power gains with some normalization – will lead to a Gamma distribution $\Gamma(M, 1/M)$ where M is the number of antennas.

In the data sets presented here, in presence of time-varying distance-dependent path gain and large-scale fading, the channel hardening effect over time is not following this theoretical distribution, in line with the analysis in [3]. Here, the small-scale fading distribution in frequency is inspected by performing MRT. For each time instant in the measurement set, i.e. $\forall k \in \{0, \dots, N_t - 1\}$, the following matrix [5], [27] is constructed

$$\mathbf{H}_k = [\tilde{\mathbf{h}}_k^{(1)}, \dots, \tilde{\mathbf{h}}_k^{(M)}] \in \mathbb{C}^{N_t \times M}, \quad (15)$$

then the MRT is computed as

$$\mathbf{H}_k^{\text{MRT}} = (\mathbf{H}_k^H \odot \mathbf{H}_k) \cdot \mathbf{1} \in \mathbb{C}^{N_t \times 1}, \quad (16)$$

without any normalization. In Fig. 14 the empirical CDF of the channel gain is plotted in log-log scale, with and without normalization such that the red curves show the channel gain including path gain, large-scale fading and small-scale fading and the blue curves only show the influence of small-scale fading, both for one and twelve antennas when using MRT. Here it can be seen that the deep dips are mitigated when combining the antennas, resulting in a steeper curve. Due to the dynamic nature of the data set there will be a varying mean power gain, but the deep dips have been mitigated. Without the normalization, large-scale fading effects are a part of the results, giving a required fading margin of not much more than 10 dB. Considering small-scale fading only, just a few dB of fading margin is sufficient for reliable communication. In either case, one can conclude that D-MIMO is indeed an enabler of ultra-reliable communication and could contribute to reduced fading margins and reduce the need of re-transmissions, also leading to reduced latencies.

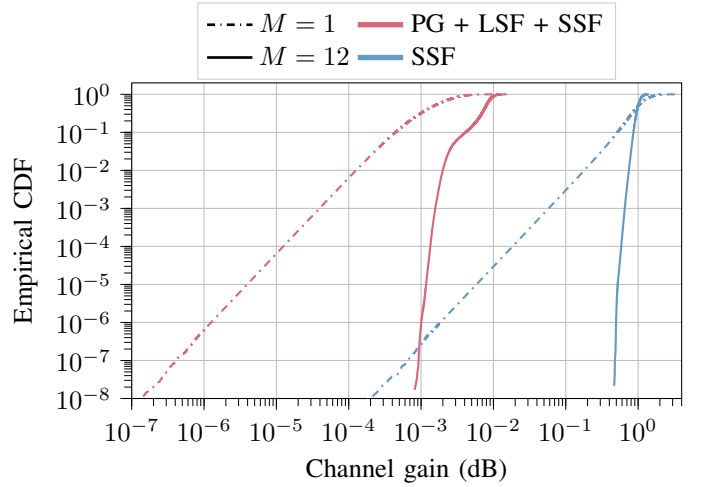


Fig. 14. The empirical CDF for the channel gain. Showing the effect with and without beamforming gain using (16). The red lines show the data under the influence of all propagation effects, i.e. path gain (PG), large-scale fading (LSF), and small-scale fading (SSF). In the blue lines the path gain and large-scale fading effects have been averaged out.

VII. A DISTRIBUTED MIMO CHANNEL MODEL FOR INDUSTRIAL ENVIRONMENTS

With all the parameters in place, here is a summary of how to apply these to generate realizations of the spatially consistent stochastic channel model, applicable for D-MIMO in industrial environments. The first step is the initialization phase:

- 1) Select the number of anchors M and place them in the environment considered.
- 2) Place the agent at its initial position in the environment.
- 3) Initialize the covariance matrix $C \in \mathbb{R}^{M \times M}$; the diagonal elements are all ones, and all off-diagonal elements are chosen as described in Sec. V-A.
- 4) For each anchor m , assign it an auto-correlation distance according to Sec. V-B.
- 5) For each anchor m , assign it a state-change probability according to Sec. III-A.
- 6) Realize and distribute N_{IO} interacting objects (IOs) for each anchor in the environment and draw an additional delay for each of them such that the power delay matches an exponential decay with an rms delay spread corresponding to Fig. 10. These IOs are then used for simulation of the small-scale fading and represent the last interaction point as seen from the agent.
- 7) Initialize the random start phases of the anchors.

The next steps are the simulation for each anchor m at time instance k :

- 1) Calculate the distance between the anchor and the agent.
- 2) Calculate the distances between the anchor, the agent, and the interacting objects.
- 3) Draw a realization to determine a potential state change between LoS and OLoS.
- 4) Calculate the deterministic path gain according to Sec. IV.

- 5) Draw a realization of the large-scale fading as in Sec. V.
- 6) Apply the large-scale fading auto-correlation distance, see Sec. V. This also applies to the instantaneous K -factor, which is determined by the link state. The large-scale fading and the K -factor are filtered by a first-order auto-regressive process where the forgetting factor k is determined by the movement of the agent in each step.
- 7) Simulate small-scale fading according to Sec. VI-C.
- 8) Apply the previously initialized covariance matrix C between all anchors.

The model is inspired by the COST 2100 framework [28] and has some similarities to this. The main addition is the extension to cover a D-MIMO scenario with correlations of large-scale fading parameters and the extraction of channel characteristics for an industrial scenario. The parameters are derived from the measured scenario with distributed single antennas in the environment. Future possible extensions are the inclusion of clusters and visibility regions of clusters and scatterers to account for antenna correlations in cases where the agent or anchors have multiple antennas. The current setup does not allow for such analysis. In the case where many antennas are used at the anchors or agent, or if a wider system bandwidth is used, the number of scatterers has to increase to match the resolvability of the system.

VIII. CONCLUSIONS

A comprehensive analysis has been conducted based on data gathered from a unique D-MIMO channel measurement campaign in an industrial environment. A new approach for classifying obstruction that is derived from lidar data and approximated from the first Fresnel zone is presented, including a state transition graph. The assumption that there are almost always (a few or several) strong links in D-MIMO systems is confirmed and a quantification based on measurement data is provided, showing what one can expect from a real scenario. Another D-MIMO characteristic paving the way for ultra-reliable communication is the increased potential for experiencing independent channels at the different antennas. Here, it is shown that there is not only a clear channel hardening effect reducing the small-scale fading effects but also, by evaluating the covariance matrix, it is established that also the large-scale fading characteristics show a diversity gain; an effect that is more prominent in LoS than in OLoS. In our scenario a 10 dB fading margin is sufficient for URLLC with negligible outage when using MRT. In dynamic D-MIMO scenarios there are both spatial and temporal non-stationarities that need to be taken into account, which are here thoroughly investigated. Finally, key channel parameters such as path gain, large-scale fading, small-scale fading, RMS delay spread are evaluated; these are essential in order to achieve an accurate channel model, for which we here provide a step-by-step recipe to achieve spatial consistency, and that can be used for system development and evaluations of D-MIMO in industrial environments.

ACKNOWLEDGMENT

The authors would like to extend their appreciation to Xuhong Li for her invaluable feedback during the data anal-

ysis. She also contributed to the measurement together with Aleksei Fedorov, Michiel Sandra, and Anders J. Johansson.

REFERENCES

- [1] ITU Recommendation M.2160-0, "Framework and overall objectives of the future development of IMT for 2030 and beyond," Nov. 2023.
- [2] L. V. der Perre, E. G. Larsson, F. Tufvesson, L. D. Strycker, E. Bjornson, and O. Edfors, "RadioWeaves for efficient connectivity: analysis and impact of constraints in actual deployments," in *2019 53rd Asilomar Conference on Signals, Systems, and Computers*. IEEE, Nov. 2019.
- [3] S. Willhammar, J. Flordelis, L. Van der Perre, and F. Tufvesson, "Channel hardening in massive MIMO: Model parameters and experimental assessment," *IEEE Open Journal of the Communications Society*, vol. 1, 2020.
- [4] J. Flordelis, X. Gao, G. Dahman, F. Rusek, O. Edfors, and F. Tufvesson, "Spatial separation of closely-spaced users in measured massive multi-user MIMO channels," in *2015 IEEE International Conference on Communications (ICC)*. IEEE, Jun. 2015.
- [5] S. Willhammar, L. V. der Perre, and F. Tufvesson, "Fading in reflective and heavily shadowed industrial environments with large antenna arrays," *IEEE Open Journal of Antennas and Propagation*, 2024.
- [6] T. S. Rappaport, S. Y. Seidel, and K. Takamizawa, "Statistical channel impulse response models for factory and open plan building radio communicate system design," *IEEE Transactions on Communications*, vol. 39, no. 5, 1991.
- [7] J. Karedal, S. Wyne, P. Almers, F. Tufvesson, and A. F. Molisch, "UWB channel measurements in an industrial environment," in *IEEE Global Telecommunications Conference, 2004. GLOBECOM'04.*, vol. 6. IEEE, 2004.
- [8] B. Holfeld, D. Wieruch, L. Raschkowski, T. Wirth, C. Pallasch, W. Herfs, and C. Brecher, "Radio channel characterization at 5.85 GHz for wireless M2M communication of industrial robots," in *2016 IEEE Wireless Communications and Networking Conference*, 2016.
- [9] D. A. Wassie, I. Rodriguez, G. Berardinelli, F. M. Tavares, T. B. Sørensen, T. L. Hansen, and P. Mogensen, "An agile multi-node multi-antenna wireless channel sounding system," *IEEE Access*, vol. 7, 2019.
- [10] Q. Zhang, T. H. Loh, D. Zhou, F. Shen, Z. Huang, and F. Qin, "A measurement campaign of industrial environment for ultra reliable IIoT systems," in *2022 14th International Conference on Wireless Communications and Signal Processing (WCSP)*, 2022.
- [11] ETSI, "TR 138 901 - V18.0.0 - 5G; Study on channel model for frequencies from 0.5 to 100 GHz," 3GPP, Tech. Rep., 2024.
- [12] A. P. Guevara, S. D. Bast, and S. Pollin, "Weave and conquer: A measurement-based analysis of dense antenna deployments," in *IEEE Int. Conf. Commun.*, Jun. 2021.
- [13] T. Choi, P. Luo, A. Ramesh, and A. F. Molisch, "Co-located vs distributed vs semi-distributed MIMO: Measurement-based evaluation," in *2020 54th Asilomar Conference on Signals, Systems, and Computers*. IEEE, nov 2020.
- [14] K. J. Jang, S. Park, J. Kim, Y. Yoon, C.-S. Kim, Y.-J. Chong, and G. Hwang, "Path loss model based on machine learning using multi-dimensional gaussian process regression," *IEEE Access*, vol. 10, 2022.
- [15] C. Nelson, X. Li, A. Fedorov, B. Deutschmann, and F. Tufvesson, "Distributed MIMO measurements for integrated communication and sensing in an industrial environment," *Sensors*, vol. 24, no. 5, Feb. 2024.
- [16] W. Xu and F. Zhang, "FAST-LIO2: Fast direct lidar-inertial odometry," GitHub, Aug. 2022.
- [17] C. Nelson and F. Tufvesson, "Raw measurement data in an industrial distributed MIMO (D-MIMO) setting," Dec. 2024. [Online]. Available: <https://doi.org/10.5281/zenodo.14502428>
- [18] T. Rappaport and C. McGillem, "UHF fading in factories," *IEEE Journal on Selected Areas in Communications*, vol. 7, no. 1, Jan. 1989.
- [19] A. F. Molisch, *Wireless communications*. John Wiley & Sons, 2012.
- [20] G. Dahman, J. Flordelis, and F. Tufvesson, "On the cross-correlation properties of large-scale fading in distributed antenna systems," in *2014 IEEE Wireless Communications and Networking Conference (WCNC)*. IEEE, Apr. 2014.
- [21] —, "Cross-correlation of large-scale parameters in multi-link systems: Analysis using the Box-Cox transformation," *IEEE Access*, 2018.
- [22] M. Gudmundson, "Correlation model for shadow fading in mobile radio systems," *Electronics Letters*, vol. 27, no. 23, Nov. 1991.
- [23] G. Matz, "On non-WSSUS wireless fading channels," *IEEE Transactions on Wireless Communications*, vol. 4, no. 5, Sep. 2005.

- [24] L. Bernadó, “Non-stationarity in vehicular wireless channels,” Ph.D. dissertation, Technische Universität Wien, 2012. [Online]. Available: <http://hdl.handle.net/20.500.12708/161119>
- [25] S. Zelenbaba, B. Rainer, M. Hofer, D. Löschenbrand, A. Dakić, L. Bernadó, and T. Zemen, “Multi-node vehicular wireless channels: Measurements, large vehicle modeling, and hardware-in-the-loop evaluation,” *IEEE Access*, vol. 9, 2021.
- [26] N. Czink, “The random-cluster model: A stochastic MIMO channel model for broadband wireless communication systems of the 3rd generation and beyond,” Ph.D. dissertation, Technische Universität Wien, 2007.
- [27] T. Lo, “Maximum ratio transmission,” *IEEE Trans. Commun.*, vol. 47, no. 10, Oct. 1999.
- [28] L. Liu, C. Oestges, J. Poutanen, K. Haneda, P. Vainikainen, F. Quitin, F. Tufvesson, and P. D. Doncker, “The COST 2100 MIMO channel model,” *IEEE Wireless Communications*, vol. 19, no. 6, pp. 92–99, 2012.



Christian Nelson received his M.Sc. degree in Engineering Physics from Lund University, Lund, Sweden in 2016. From 2013 to 2016 he was working with simulations and measurements in electronic warfare at the Swedish Defense Research Agency (FOI), in Linköping, Sweden. He is currently pursuing a Ph.D. in electrical engineering and wireless communication with the Department of Electrical Engineering and Information Technology, Lund University. His research interests include signal processing, software-defined radio design, and radio-based

localization.



Sara Willhammar received her dual Ph.D. degree in Electrical Engineering from Lund University, Sweden, and KU Leuven, Belgium, in 2023. Currently, she is a postdoctoral fellow in the Department of Electrical and Information Technology at Lund University, Sweden. Her main research interests are channel measurements, characterization, and modeling in order to improve reliability and efficiency in MIMO-based systems.



Fredrik Tufvesson received his Ph.D. in 2000 from Lund University in Sweden. After two years at a startup company, he joined the department of Electrical and Information Technology at Lund University, where he is now professor of radio systems. His main research interest is the interplay between the radio channel and the rest of the communication system with various applications in 5G/B5G systems such as massive MIMO, mm wave communication, vehicular communication and radio-based positioning. Fredrik has authored around 110 journal papers

and 175 conference papers, he is fellow of the IEEE and his research has been awarded with the Neal Shepherd Memorial Award (2015) for the best propagation paper in IEEE Transactions on Vehicular Technology, the IEEE Communications Society best tutorial paper award (2018, 2021) and the IEEE Signal Processing Society Donald G. Fink overview paper award 2023.